

Machine Learning Changes the Rules for Flux Limiters

Nga Nguyen-Fotiadis,¹ Michael McKerns,¹ and Andrew Sornborger¹

¹*Information Sciences, CCS-3, Los Alamos National Laboratory, Los Alamos, NM 87545, USA*

Learning to integrate non-linear equations from highly resolved direct numerical simulations (DNSs) has seen recent interest due to the potential to reduce the computational load for numerical fluid simulations. Here, we focus on a specific problem in the integration of fluids: the determination of a flux-limiter for shock capturing methods. Focusing on flux limiters learned from data has the advantage of providing specific plug-and-play components for existing numerical methods. Since their introduction, a large array of flux limiters has been designed. Using the example of the coarse-grained Burgers' equation, we show that flux-limiters may be rank-ordered in terms of how well they integrate various coarse-grainings. We then develop theory to find an optimal flux-limiter and present a set of flux-limiters that outperform others tested for integrating Burgers' equation on lattices with $2\times$, $3\times$, $4\times$, and $8\times$ coarse-grainings. Our machine learned flux limiters have distinctive features that may provide new rules-of-thumb for the development of improved limiters. Additionally, we optimize over hyper-parameters, including coarse-graining, number of discretized bins, and diffusion parameter to find flux limiters that are best on average and more broadly useful for general applications. Our study provides a basis for understanding how flux limiters may be improved upon using machine learning methods.

I. INTRODUCTION

Numerically integrating fluid equations on a coarse grid relative to a fully resolved integration of a given problem (coarse-graining) has been of interest for many years [1, 2] since it can significantly reduce the computational time required for a given simulation. With the advent of modern machine learning methods, a number of attempts have been made to develop improved coarse-grained models, including for 3D Eulerian [3] and Navier-Stokes turbulence [4], buoyancy-driven, variable density turbulence [5], and molecular-level simulations [6].

In this paper, our focus will be machine learning an accurate local integrator for the coarse-grained, 1-D viscous Burgers' equation [7]. Burgers' equation is the simplest fluid equation admitting shocks [8, 9] and is exactly integrable. Numerically integrating shocks is complicated by the Gibbs effect [10], where, when a discontinuity develops, unstable oscillations develop in a numerical simulation. This behavior may be corrected using shock capturing methods [11–15]. Shock capturing methods rely on *flux limiters* - non-linear interpolations between high- and low-resolution integration schemes used in a numerical simulation to keep a shock solution monotonic, thereby eliminating spurious oscillations.

Harten [14] provided a framework for constructing non-linear, monotonicity preserving flux limiters. At present, a large number of flux limiters have been defined and used in the literature [16]. Different forms of flux limiter have been shown to have differing accuracy and convergence performance [16]. And criteria have been studied for determining what parameter regions are appropriate for different classes of limiter [17].

Since Burgers' equation is exactly integrable, it is straightforward to generate accurate, high-resolution data from which flux limiters may be tested using a machine learning approach. This setting also provides a good testing ground for developing methodology and evaluating which flux limiters are the best (for one particular equation, or potentially for multiple shock-forming equations), and for comparing existing flux limiters with those learned from data.

Below, we will introduce the Cole-Hopf solution to the inviscid Burgers' equation, show how to use it to test DNS training data, and define our flux limiters. We will then present a cost function

allowing us to compare predicted outcomes from a discretized flux limiter with high-resolution DNS training data. Next, we will optimize the cost function for a given set of data resulting in a regression analysis solvable with standard linear algebraic methods. We then apply this analysis to a training dataset to learn optimal flux limiters from coarse-grained data. We compare these optimized, coarse-grained flux limiters with a large set of other flux limiters and show that they outperform them over the set of coarse-grainings. We finally incorporate our regression analysis within a larger, hyper-parameter optimization framework to find an optimal discretization of the flux limiter over a range of parameters, including coarse-graining, number of discretization bins, and diffusion parameter.

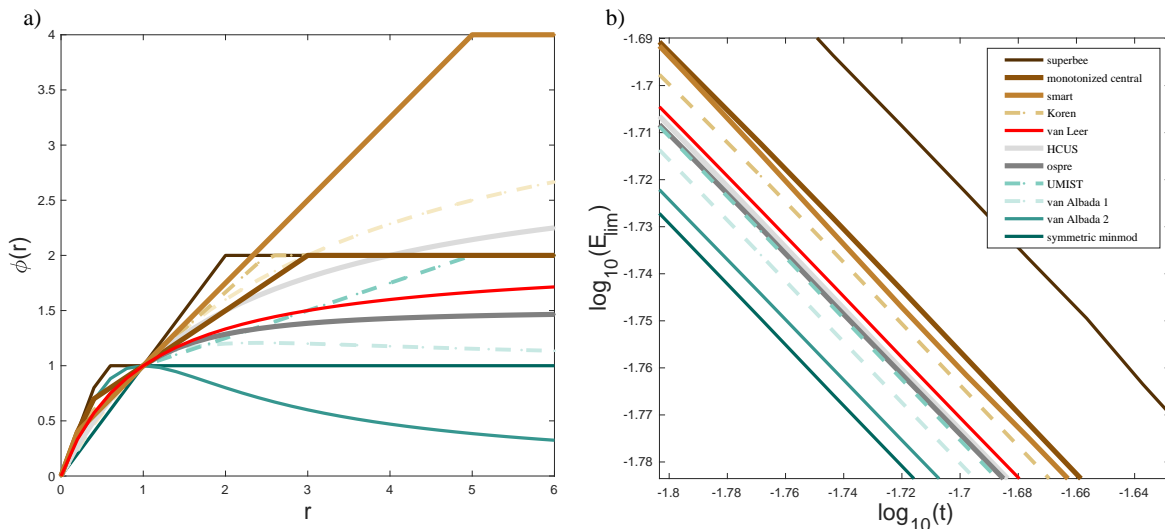


FIG. 1. a): 11 flux limiters, $\phi_i(r)$, where i ranges over a set of standard flux limiters (see legend in b)), plotted as a function of flux ratio r . All flux limiters, by design [17], go through the point, $(r, \phi) = (1, 1)$. b): Log-error computed for each standard limiter in a) with error, $E_{\text{lim}} = e_i - e_{\text{hres}}$, with e_i the shock capturing solution with limiter, i , and e_{hres} the $2\times$ coarse-grained high-resolution solution. Here, and in Figures below showing comparisons in time, we compare against the standard sinusoidal solution of Burgers' equation. Note that while most limiters are bowed out below $r < 1$, the better performing (lower error, in green) limiters tend to be comparatively (with regard to van Leer, in red) bent down for $r > 1$.

II. BACKGROUND

A. Exact Solution of Inviscid Burgers' Equations

The viscous Burgers' equation [7] written in conservative form is

$$\frac{\partial u}{\partial t} + \frac{\partial}{\partial x} \left(\frac{u^2}{2} - \nu \frac{\partial u}{\partial x} \right) = 0. \quad (1)$$

It may be solved exactly with the Cole-Hopf transform [9],

$$u = -2\nu \frac{1}{\phi} \frac{\partial \phi}{\partial x}. \quad (2)$$

For periodic boundary conditions (those considered here), the transform results in a diffusion equation

$$\frac{\partial \phi}{\partial t} = \nu \frac{\partial^2 \phi}{\partial x^2}, \quad (3)$$

which may be solved with Fourier methods. Finally, the Cole-Hopf transform is inverted to recover the solution in the original coordinates.

We used a discretized version of the Cole-Hopf transform on a finely resolved lattice to generate simulation data. This approach works well for moderately sized lattices, but has instabilities for larger lattices when ν becomes small [18]. Thus, for our flux limiter optimization procedure, below, we used a first-order, but very accurate scheme to generate our training and test data and validated the scheme, which is stable for any sized lattice, on simulations on smaller lattices by comparing with the discretized Cole-Hopf transform (See Appendix A). We call data generated in this way *exact* or *high-resolution* data. Note that this solution method can resolve shocks without the need for flux limiters and thus provides good data to test flux limiters in shock capturing integration schemes. For equations with no analytical solution, high-resolution data from finely resolved DNSs would need to be used.

B. Flux Limiters

We use a semi-discrete scheme to integrate initial conditions from coarse-grained data selected at different resolutions from previously generated exact data. The integration scheme takes the general form

$$\frac{du_i}{dt} + \frac{1}{\Delta x_i} \left[G\left(u_{i+\frac{1}{2}}\right) - G\left(u_{i-\frac{1}{2}}\right) \right] = 0. \quad (4)$$

Here, i is a cell index, and $G\left(u_{i-\frac{1}{2}}\right)$ and $G\left(u_{i+\frac{1}{2}}\right)$ denote edge fluxes. The edge fluxes are non-linear interpolations between high- and low-resolution fluxes

$$G\left(u_{i+\frac{1}{2}}\right) = (1 - \phi(r_i)) f_{i+\frac{1}{2}}^{\text{low}} + \phi(r_i) f_{i+\frac{1}{2}}^{\text{high}}, \quad (5)$$

$$G\left(u_{i-\frac{1}{2}}\right) = (1 - \phi(r_{i-1})) f_{i-\frac{1}{2}}^{\text{low}} + \phi(r_{i-1}) f_{i-\frac{1}{2}}^{\text{high}}. \quad (6)$$

Here, f^{low} indicates a low-resolution flux, typically first-order, which does not suffer from Gibbs phenomena, and f^{high} indicates a high-resolution flux to integrate smoother regions of a solution. The flux limiter, $\phi(r)$, is a function of the flux ratio,

$$r_i = \frac{u_i - u_{i-1}}{u_{i+1} - u_i}. \quad (7)$$

A large number of flux limiters have been proposed and used. For instance, the van Leer flux limiter [19] takes the form

$$\phi(r) = \frac{r + |r|}{1 + |r|}. \quad (8)$$

Note that this flux limiter and all of the flux limiters that we consider (see Fig. 1 and Tab. VII) here are (piecewise) continuous and zero for $r \leq 0$.

III. METHODS

A. A Shock Capturing Integration Method for Burgers' Equation

For low- and high-resolution, we chose Lax–Friedrichs (LF)

$$f_{i\pm\frac{1}{2}}^{\text{low}} = f_{i\pm\frac{1}{2}}^{\text{LF}} = \frac{1}{2}[F(u_i) + F(u_{i+1}) \mp \alpha \frac{\Delta x}{\Delta t}(u_{i\pm 1} - u_i)]; \quad \alpha = \max_u \left| \frac{\partial F}{\partial u} \right| \quad (9)$$

and Lax–Wendroff (LW) fluxes

$$f_{i\pm\frac{1}{2}}^{\text{high}} = f_{i\pm\frac{1}{2}}^{\text{LW}} = \frac{1}{2}[F(u_i) + F(u_{i+1}) \mp \frac{\Delta t}{\Delta x} \left(\frac{\partial F}{\partial u}(u_{i\pm\frac{1}{2}}) \right) (F(u_{i\pm 1}) - F(u_i))], \quad (10)$$

where $F = \frac{u^2}{2} - \nu \frac{\partial u}{\partial x}$ is the flux from Burgers' equation. Eq. (4) now becomes:

$$u_i(t_{n+1}) = u_i(t_n) - \frac{\Delta t}{\Delta x} \Delta F^i \quad (11)$$

with

$$\Delta F^i = \Delta F_1^i + \phi(r_i) \Delta F_2^i + \phi(r_{i-1}) \Delta F_3^i, \quad (12)$$

where ΔF_1^i , ΔF_2^i , and ΔF_3^i can be written explicitly as:

$$\begin{aligned} \Delta F_1^i &= f_{i+\frac{1}{2}}^{\text{LF}} - f_{i-\frac{1}{2}}^{\text{LF}}, \\ \Delta F_2^i &= f_{i+\frac{1}{2}}^{\text{LW}} - f_{i+\frac{1}{2}}^{\text{LF}}, \\ \Delta F_3^i &= -(f_{i-\frac{1}{2}}^{\text{LW}} - f_{i-\frac{1}{2}}^{\text{LF}}). \end{aligned} \quad (13)$$

In Fig. 1(a), we plot a set of 12 different flux-limiters from the literature. An important feature to note in these flux limiters is that they all pass through the point $\phi(1) = 1$. This is due to a requirement of second-order accuracy of the shock capturing scheme and Lipschitz continuity of $\phi(r)$ [17]. In Fig. 1(b), we show the difference between solutions computed with the various flux limiters and high-resolution data. In this example, both simulation and high-resolution data are coarse grained at $2\times$ (i.e. initial conditions for each simulation were subsampled at every other grid point from high-resolution data, integrated with a shock-capturing scheme for time t , then compared to subsampled high-resolution data at time t). In (Fig. 1(b)), we see an ordering where some flux limiters perform better than others for predicting coarse-grained data. Note that, although we plot the errors over a short time, the errors retain the same ordering over the whole integration. Thus, we can define an ordering of the limiters.

At this point, the question as to what the optimal flux limiter is arises. In this study, we set up the problem of how to find a flux limiter, $\phi(r)$, that is optimal with respect to certain criteria. We will train a piecewise linear flux limiter using an exact dataset (Appendix A) and compare it with the 11 flux limiters shown in Fig. 1(a).

B. Flux Limiter Discretization

We discretize the flux-limiter that we will optimize with machine learning methods, $\phi(r)$, in piecewise linear segments, where the k 'th segment has the form,

$$\phi_k(r) = \phi_0 + b_1(r_2 - r_1) + b_2(r_3 - r_2) + \dots + b_k(r - r_k) + 0_{k+1} + \dots + 0_K, \quad (14)$$

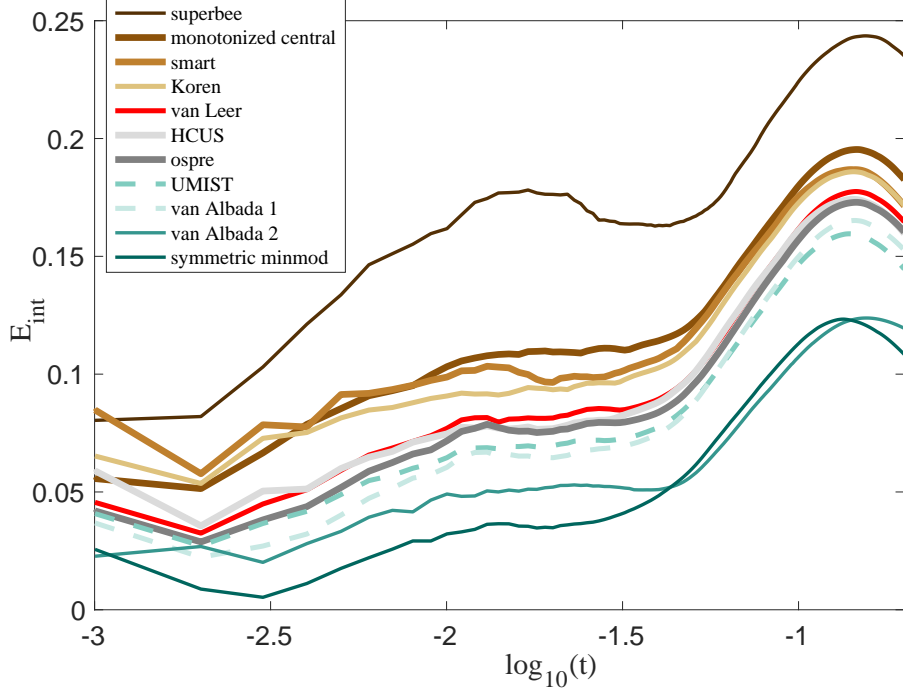


FIG. 2. Learning a $2\times$ coarse-grained flux limiter. Relative error integrated across the spatial dimension, E_{int} , calculated for a set of standard flux limiters using $K = 20$ bins versus $(\log \text{ of })$ time. Note that, compared to all standard limiters, the $2\times$, $K = 20$ bin learned limiter performs better. Also, note that, similarly to what we saw in Fig. 1, the standard limiters are ordered with respect to their performance.

and $r \in [r_k, r_{k+1})$, $k \in \{1, \dots, K\}$, $\phi_0 = 0$, and b_i are slope coefficients. Note that for $r \leq 0$, $\phi(r) = 0$ and for $r = r_K$, all terms in Eq. (14) are non-zero. Below, we use vector notation, $\mathbf{b} = [b_1, b_2, \dots, b_k, b_{k+1}, \dots, b_K]^T$ for slope coefficients. Eq. (14) can be rewritten as $\phi_k(r) = \mathbf{b}^T \Delta \mathbf{r}_k$ with $\Delta \mathbf{r}_k$ defined as

$$\Delta \mathbf{r}_k = [r_2 - r_1, r_3 - r_2, \dots, r - r_k, 0, \dots, 0]^T. \quad (15)$$

C. Learning an Optimal Discretized Flux Limiter

To optimize the discretized flux-limiter in Eq. (14), we define the mean squared error between N input-output pairs, $\{o_i(\{u_c^i\}), g_i\}$:

$$C = \frac{1}{2} \sum_{i=1}^N (o_i(\{u_c^i\}) - g_i)^2 \quad (16)$$

as the cost. Here, g_i is the high-resolution fluid velocity at the i -th grid position at time t_{n+1} and o_i is the shock-capturing method's prediction of the fluid velocity at time t_{n+1} from data at the previous timestep. o_i is a functional of a subset of data points $\{u_c^i\} = \{u_c^{i1}, u_c^{i2}, u_c^{i3}, \dots, u_c^{iN_c}\}$ indicated relative to the i -th grid position at time step t_n . Here, we used $N_c = 6$ data points at time t_n (see details in Appendix B) to predict a data point g_i at t_{n+1} , i.e. $\{u_c^i\} = \{u_{i-3}, u_{i-2}, u_{i-1}, u_i, u_{i+1}, u_{i+2}\}$. Thus, $o_i(\{u_c^i\})$ is the integration obtained with the flux-limiter method defined in Eqs. (4), (9), (10), (14) given a set of 6-points $\{u_c^i\}$:

$$o_i(\{u_c^i\}, t_{n+1}) = u_i(t_n) - \frac{\Delta t}{\Delta x} \Delta F(\{u_c^i\}, \{b_i\}, t_n). \quad (17)$$

Here, $\Delta F(\{u_c^i\}, \{b_i\}, t_n)$, defined via Eqs. (12) and (13), is the difference of the two fluxes defined in Eq. (4). The minimum of the cost function, Eq. (16), can be computed exactly by finding the unique root, \mathbf{b} , of the equation $\frac{\partial L}{\partial \mathbf{b}} = \mathbf{0}$, that is:

$$\sum_{i=1}^N \left(u_i - g_i - \frac{\Delta t}{\Delta x} \Delta F^i \right) \left(-\frac{\Delta t}{\Delta x} \right) \Delta \mathbf{s}_i \Delta \mathbf{F}_{2,3}^i = \mathbf{0}. \quad (18)$$

In Eq. (18), $\Delta F^i = \Delta F(\{u_c^i\}, \{b_i\}, t_n)$ is defined via Eqs. (12) and (13). $\Delta \mathbf{s}_i = [\Delta \mathbf{r}_i, \Delta \mathbf{r}_{i-1}]$ is a $K \times 2$ matrix with $\Delta \mathbf{r}_i$ defined in Eq. (15). $\Delta \mathbf{F}_{2,3}^i = [\Delta F_2^i, \Delta F_3^i]^T$ with components ΔF_2^i and ΔF_3^i defined via Eq. (13).

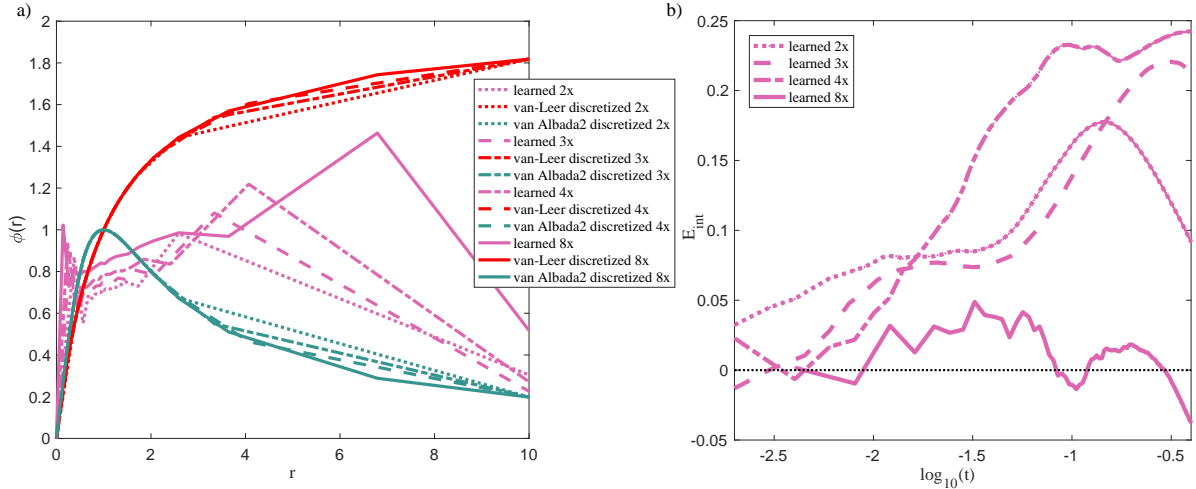


FIG. 3. (a): $K = 20$ bin machine learned limiter functions $\phi(r)$, van Leer, and van Albada 2 limiters plotted using the same discretized bins from 4 different coarse grained cases: $2\times$, $3\times$, $4\times$, and $8\times$. (b): Corresponding integrated relative errors, E_{int} (20), between the learned flux limiters with van Leer as a function of (log) time as compared to the ground truth for $2\times$, $3\times$, $4\times$, and $8\times$. Note that the machine learned limiters are not constrained to go through $(r, \phi) = (1, 1)$ (and, in this case, they do not).

Solving Eq. (18) reduces to solving a linear equation $\mathbf{A} \cdot \mathbf{b} = \mathbf{C}$ that yields $\mathbf{b} = \mathbf{A}^{-1} \cdot \mathbf{C}$. Here, $\mathbf{A} = \Delta \mathbf{r}_F \cdot (\Delta \mathbf{r}_F)^T$ and $\mathbf{C} = \frac{\Delta x}{\Delta t} \sum_{i=1}^N O_G^i \Delta \mathbf{r}_F^i$, where $\Delta \mathbf{r}_F$ is a $K \times N$ matrix with each column $\Delta \mathbf{r}_F^i$ a $K \times 1$ vector defined as $\Delta \mathbf{r}_F^i = (\Delta \mathbf{s}_i)(\Delta \mathbf{F}_{2,3}^i)$. Finally, $O_G^i = u_i - g_i - \frac{\Delta t}{\Delta x} \Delta F_1^i$. Note that ΔF_1^i is defined via Eq. (13) and we recall that K is the size of the discretized flux limiter (i.e. the size of \mathbf{b}). Hence, each matrix \mathbf{A} (or \mathbf{C}) is a function of N training data points.

We wish our estimates of each segment of the flux limiter, $\phi_k(r)$, to have the same variance. Choosing this discretized space wisely is an important step. Our choice was to discretize the flux limiter such that each segment contained an equal number of training data points.

We used the above method with different coarse-grainings of the high-resolution dataset as training data in order to find optimal flux limiters, $\phi_k(r)$, for a set of coarse-grainings.

D. Hyperparameter Optimization of a Discretized Flux Limiter

The cost function defined in the previous section is intended to optimize a discretized flux-limiter for a given coarse-graining, CG , number of bins, K , and diffusion parameter, μ . We automated the generation of training and test data, the training of a discretized flux-limiter, and the testing of the learned limiter, to yield a function that produces the cost C as defined in Eq. (16) for

a given CG , K , and μ . This approach leads to very good flux limiters for a particular set of parameters, however, the question remains as to whether we can find limiters that function well in a more general context. To attack this issue, we extended our approach by optimizing over (hyper)parameters. By averaging the cost for a learned flux-limiter over all segments,

$$\bar{C} = \sum_{k=1}^K C_k / K . \quad (19)$$

In particular, we used an optimizer to produce a flux-limiter that minimizes \bar{C} within the region defined by $\mu \in [0.01, 0.5]$, $CG \in [2, 10]$, and $K \in [2, 30]$.

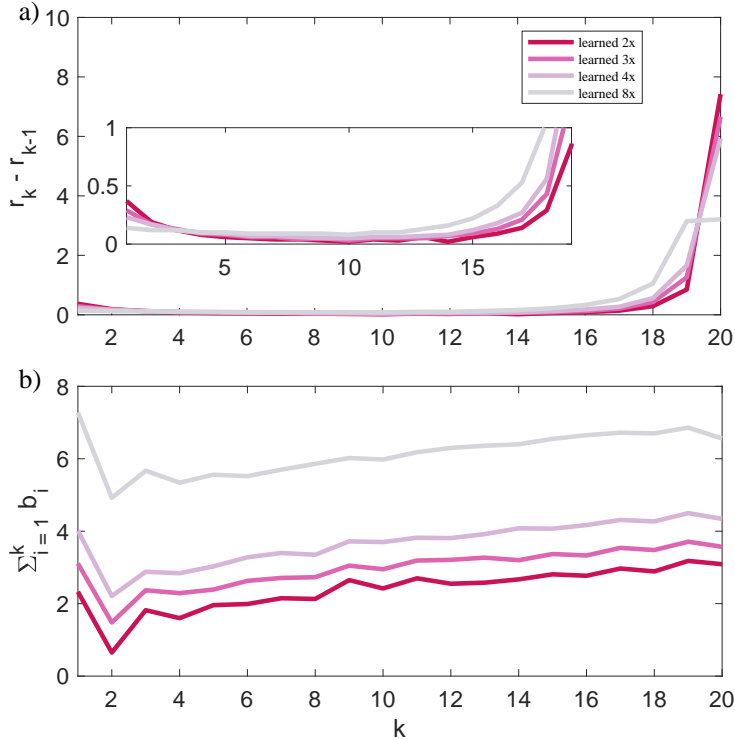


FIG. 4. Patterns in the scaling of learned flux limiters. a) Bin widths vs. k . Note the inversion of bin widths from left to right. Larger coarse grainings have smaller bin widths close to $r = 0$ and vice-versa for large r . b) The cumulative sum of the slopes, $\sum_{i=1}^k b_i$. This function has the same form across coarse-grainings but scales as a function of coarse-graining. Note also that b_1 is proportional to the coarse-graining, and the bulk of the k points occur in the roughly linear region with low-amplitude fluctuations ($r \in [0.5, 2.0]$) in Fig. 3(a).

IV. RESULTS

We generated 500 Burgers' simulations with 500 random initial conditions that have in total 160M data points. We attained good convergence of training results even with just 80 simulations (i.e. using less than 30M data points). For a discretization into 20 segments, the solution to \mathbf{b} was estimated with 1.5M data points per element and hence had a standard error of 0.0008. For this case, diagonalization was performed on the inverse of the square matrix \mathbf{A} of size $K \times K$ with

maximal K being $K = 20$ segments. Better standard errors were obtained with fewer segments, but at the cost of worse resolution of the limiter.

We validated our learning model on a subset of hold-out data which contained samples, $\{u_c^i\}$, from about 20 simulations.

We compared our optimized flux limiter with a set of standard flux limiters (sFLs). We computed the spatially integrated relative error

$$E_{\text{int}} \equiv \sum_i \left(\frac{e_i^{\text{sFL}} - e_i^{\text{learned}}}{e_i^{\text{learned}}} \right), \quad (20)$$

where the error at a given grid location, i , for each flux limiter is

$$e_i = o_i - g_i. \quad (21)$$

Note that this error, as defined, is positive when the learned limiter outperforms a given sFL. We investigated $K = 2, 5$, and 20 segment flux limiters. Optimized flux limiters for all values of K were better than the discretized van Leer limiter (i.e. the relative error was everywhere > 0 with an average improvement of about 10%).

In Fig. 2, we plot the integrated relative error of our optimized flux limiter with $K = 20$ versus a set of eleven sFLs. Here, CG is $2\times$ and $r \in [0.0, 10.0]$. Note that the optimized limiter performs better than all other limiters investigated. Here, the symmetric minmod limiter performs best, but still reaches 10% greater error relative to the optimized limiter.

We plot optimized limiters, $\phi_k(r)$ in Fig. 3(a). Also, included in the plot are van Leer and

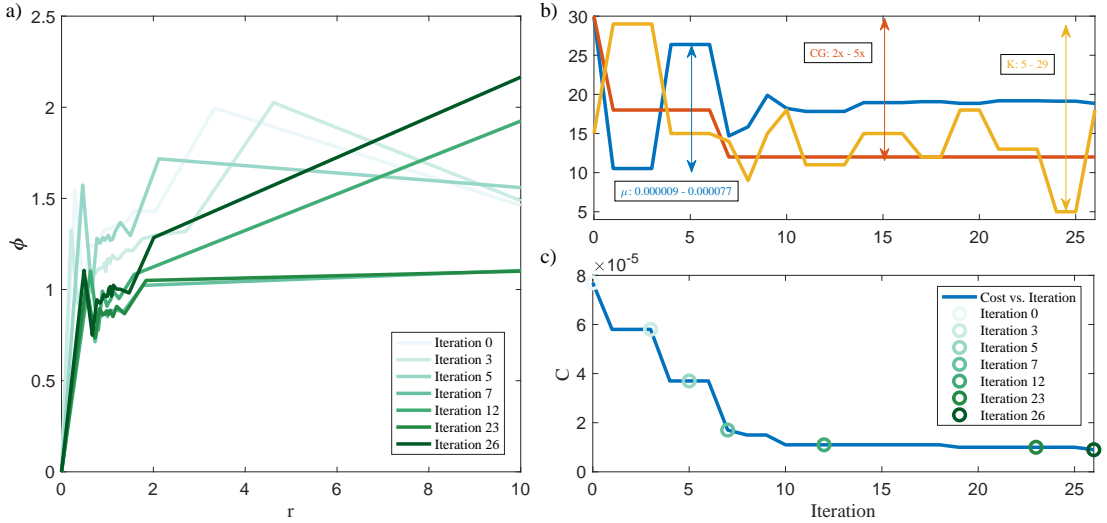


FIG. 5. Finding optimal flux limiters across multiple hyperparameters. a) A sequence of flux limiters learned over multiple iterations of optimization. The legend indicates the coarse-graining and the number of bins for which the flux limiter performs best, and the iteration at which it was found. b) Parameter convergence vs. iteration. Double headed arrows indicate the scale of parameter variation. Number of bins (yellow), coarse graining (red), diffusion parameter, μ (blue). c) The cost as a function of iteration. Circles denote iteration steps for flux limiters plotted in a). Note, in comparing b) and c), that convergence of the cost is primarily driven by μ , while K appears to have no effect.

van Albada 2 limiters for reference. These two limiters are commonly-used limiters and bound the learned $K = 20$ limiters. For this analysis, equal-variance bins (see Sec. III C) were computed

individually for coarse grainings of $2\times$, $3\times$, $4\times$, and $8\times$ (transitioning from dotted to solid magenta lines in Fig. 3(a)). Note that the smallest coarse grained case ($2\times$) has the smallest first slope b_1 in the first linear piece of $\phi(\{b_i\}, r)$, see Table I. As we increase the coarse graining to a value larger

Coarse graining	$2\times$	$3\times$	$4\times$	$8\times$
First slope	2.33	3.11	4.02	7.28

TABLE I. First slope b_1 of the flux limiter obtained for 4 different coarse grainings shown as 4 solid lines in Fig. 3(a). Note that b_1 approximates the coarse-graining.

than $2\times$, we see an increase in the slope of this first segment where b_1 roughly tracks the value of the coarse-graining.

In Fig. 3(b), we show errors, E_{int} , relative to the van Leer limiter, as a function of time, t . Note that for $2\times$ through $8\times$ coarse grainings, the optimized limiters perform best, but for $10\times$ (not plotted in (a)), the discretized van Leer limiter performs better. Note that here, we compare with the continuous van Leer limiter.

Upon inspection of Fig. 3, the general form of the learned limiters is 1) an initial (small r) sharply sloped kink that gets sharper as coarse-graining increases, 2) a subsequent roughly linear region with low-amplitude fluctuations, and 3) a final (large r) kink that is less sharply sloped than the initial kink. In Fig. 4, we visualize this pattern by plotting the bin widths (Fig. 4(a)) and integrated slopes (Fig. 4(b)), $\sum_{i=1}^K b_i$. The main patterns to point out here are that bin widths decrease for small r and increase for large r , while the integrated slopes are virtually identical as a function of coarse-graining, with the exception that they scale roughly with the coarse-graining. Note also (in Tables II and III) that $r_k \sim 1.0$ when $k \sim K/2$, $r_K \sim CG$, and $b_1 \sim CG$.

Fig. 5 demonstrates the outcome of a flux limiter optimization in the hyperparameter subspace, $\{CG, K, \mu\}$, defined in Sec. III D. For this optimization, we selected the Differential Evolution [20] optimizer from *mystic* [21, 22] with the coarse-graining and number of bins restricted to be integers. A population of twenty-two initial points (CG, K, μ) , chosen at random from within the set of valid solutions, was mutated at each iteration. Thus, each new generation contained twenty-two candidate solutions per iteration. The optimizer continued to generate new candidate solutions until the change in candidate solutions was less than 10^{-10} over 100 iterations. We selected *mystic* in part due to the ability to perform accurate optimizer restarts. Accordingly, we used 100 simulations to build each training set, and 20 simulations for each test set, for the first twelve (or so) iterations. Restarts beyond the twelfth iteration used 12 simulations for each training set and 3 simulations for each test set. Each simulation was run for $t = 800$ seconds. New training (and test) data is generated for each new combination of (CG, K, μ) as part of the automated procedure.

In Fig. 5(a), we plot the learned flux limiters at select iterations as the hyperparameters converge. Note that as the learned limiters improve (with regard to the cost, in Fig. 5(c)), there is a convergence onto a positive linear slope at large r , and a convergence of the mid-segment $r_{K/2}$ of the limiter to roughly $(r, \phi) = (1, 1)$. In comparing Fig. 5(b) and Fig. 5(c), it is apparent that the convergence of the cost is primarily driven by the convergence of the diffusion parameter, μ , and secondarily the coarse-graining, CG , while the number of bins, K , has little effect (also see Table IV). The lack of dependence of the cost on K makes sense, given that for all learned discretized flux limiters, the bulk of the line segments, r_i , occur in the roughly linear region, $r \in [0.5, 2.0]$, where the slope b_i exhibits only low-amplitude fluctuations. Essentially, as long as K is large enough to produce the initial and final kinked segments, any remaining extraneous segments appear to condense in the roughly linear region around $r = 1$.

It also appears that in later iterations, where CG is fixed and μ is still converging, that the value of μ may have a large impact on the shape of the limiter through ϕ_K and the slope b_K for the

last line segment. In early iterations, where CG and μ are not nearly converged, we can see that at the mid-segment $r_{K/2} = 1.0$, but $\phi_{K/2} \neq 1.0$. As CG and then μ converge, we find $(r, \phi) = (1, 1)$.

The flux limiters learned at select iterations during the hyperparameter optimization are given in Tables V and VI, and very roughly follow the ‘rules’ established for r and b in Tables II and III. Specifically, learned limiters have an initial kinked region with a large slope, a final kinked region with a smaller slope, and a smaller roughly linear region around $r_k \sim 1.0$ when $k \sim K/2$. Additionally, we see that generally $r_K \sim CG$ and $b_1 \sim CG$, however these rules are a bit less tightly adhered to in Tables V and VI, likely due to poor convergence of the learned limiter at certain iterations and/or the use of significantly fewer simulations in the training and test sets.

V. DISCUSSION

Here, we presented a framework for the data-driven determination of optimal flux limiters for the coarse-grained Burgers’ equation. The framework consists of an internal optimizer computable with numerical linear algebraic methods, which can optionally be further optimized via a hyperparameter search over problem-specific parameters such as the number of bins in the limiter, the coarse-graining of the data, and the diffusion parameter (for Burgers’ equation this is the only physical parameter in the problem).

By focusing on optimizing flux limiters, we attacked a central component of shock-capturing methods for integrating fluids. This allows our flux limiters to be essentially plug-and-play components for many existing numerical codes. We caution, however, that further work must still be done to understand how generally valuable our results are for fluid equations other than Burgers’. Information as to whether and how the regularities discovered in learned limiters change dependent on the target system may be useful for understanding the structure of shock-capturing codes more generally.

We chose to measure the quality of a discretized flux limiter by minimizing the mean-squared misfit for the limiter using 6-grid point segments from the training data, averaged over all segments (as in Eq. (19)). We showed that under this condition, when searching for a generally optimal limiter across a range of hyperparameters, flux limiters should be designed with the following rules-of-thumb: they should have 1) a fixed point at $(r, \phi) = (0, 0)$, 2) a first segment with a slope of $b_1 \sim CG$, 3) a second segment with a negative slope $b_2 < 0.0$ followed by 4) a roughly linear region around $(r, \phi) = (1, 1)$ and $k \sim K/2$, and 5) a larger final region where $r_K \sim CG$. However, when focusing on specific coarse-grainings (not generally optimal), it is interesting to note that the $(r, \phi) = (1, 1)$ constraint, which is due to a requirement of second-order accuracy of the shock capturing scheme and Lipschitz continuity of ϕ [17], is not obeyed, yet these limiters, nonetheless, perform better than standard limiters.

A main advantage of our limiters seems to be the flexibility allowed by the multiple segments that make up their shape. As opposed to the bent or bowed shapes of standard limiters, multiple segment limiters allow a spring-like compression that, at least for Burgers’ equation, allows for an improvement in their performance.

Given the rules-of-thumb that we have observed, our results for finding an optimal limiter over the range of $CG \in [2, 10]$, $K \in [2, 30]$, and $\mu \in [0.01, 0.5]$, could most likely be improved by fixing the number of bins K , constraining the limiter to follow the rules noted above, and rerunning using a number of simulations N_s similar to that used when solving for a fixed (CG, K, μ) .

For fixed (CG, K, μ) calculations, we used $N_s = 500$ with 500 random initial conditions, yielding in total 160M data points. For variable (CG, K, μ) calculations, we used $N_s = 100$ with 100 random initial conditions, using less than 30M data points. We used a smaller N_s for the hyperparameter calculations to help reduce the computational cost of training the limiter, at the expense of some

accuracy in the learned flux limiter. We performed our calculations on the Darwin cluster at Los Alamos National Laboratory on a 22 core cluster, where simulations were run in parallel, one simulation per core.

The first 12 iterations in the hyperparameter optimization completed in just less than 48 hours, with restarts (i.e. further optimization runs) performed over the next several days. Fixing K , and using a larger number of parallel cores, should be able to decrease the time to obtain results. It appears we may be able to fix the number of bins at $K \sim 6$, and while better standard errors per bin are obtained with fewer segments, the price is worse resolution of the limiter. It may be interesting to attempt to learn a relationship between the minimum number of bins required, the resolution of the limiter, and the resulting standard error. Another interesting study may be to discover the impact on the observed set of rules when $N_c \neq 6$, and if it has any impact on the shape or minimum number of bins.

Another interesting observation is that while we used a diffusion parameter of $\nu = 0.01$ in our simulations, we found a learned diffusion parameter of $\mu = 0.047$ in our hyperparameter optimization (see Table IV). The difference is a factor of 2, which counter-balances the difference in coarse-graining between our simulations and the learned limiter. Similar changes in effective diffusion are seen in analytical approaches to coarse-graining [1, 2]. It may be prudent to determine if the diffusion parameter can always be determined similarly for other choices of CG.

Here, we chose to develop and test our machine learning approach to discovering improved flux limiters using 2nd order shock-capturing methods. State-of-the-art methods such as the piecewise-parabolic methods [13, 23] (PPM, 4th order) or (weighted) essentially non-oscillatory [24–26] (ENO, WENO, 8th order) methods may also benefit from our machine learning approach.

Further, as the generation of training data contains some randomness, an improvement would be to modify Eq. (16) to train flux limiters that minimize the expected mean squared error between input-output pairs:

$$C = \frac{1}{2} \sum_{i=1}^N \mathbb{E}(o_i(\{u_c^i\}) - g_i)^2 . \quad (22)$$

In our study the impact of the randomness in the training data is mitigated by using a large number of simulations. Thus, we may be able to use significantly fewer simulations if we instead train the limiter on the expected mean-squared error. Additionally, our approach could be used to train flux limiters for *robustness* by minimizing \overline{C} , defined as:

$$\overline{C} = \sum_{k=1}^K \max C_k / K , \quad (23)$$

for a range of (CG, μ) , with C_k defined as in Eq. (22).

VI. ACKNOWLEDGEMENTS

We thank Daniel Livescu for helpful discussions. Research presented in this article was supported by the NNSA’s Advanced Simulation and Computing Beyond Moore’s Law Program at Los Alamos National Laboratory, and by the Uncertainty Quantification Foundation under the Statistical Learning program. Los Alamos National Laboratory is operated by Triad National Security, LLC, for the National Nuclear Security Administration of the U.S. Department of Energy (Contract No. 89233218CNA000001). The Uncertainty Quantification Foundation is a nonprofit dedicated to the advancement of predictive science through research, education, and the development and dissemination of advanced technologies. This document’s LANL designation is LA-UR-21-28444.

A. HIGH-RESOLUTION SOLUTIONS

In this Appendix, we discuss the solution obtained with a high-resolution, first-order scheme that we use to generate training and testing data, as compared to the discretized Cole-Hopf approach. We note again that the Cole-Hopf approach may exhibit instability when ν is small. The explicit form of the high-dimensional solution to Eq. (4) was obtained numerically as:

$$u_i(t_{n+1}) = u_i(t_n) + \Delta t(\mathbf{D}\mathbf{v} + \mathbf{G}\mathbf{v}^2) \quad (24)$$

with $\mathbf{D} = \frac{1}{(4\Delta x)}[1, 0, -1]$, $\mathbf{v} = [u_{j-1}, u_j, u_{j+1}]^T$, and $\mathbf{G} = \frac{\nu}{(\Delta x^2)}[1, -2, 1]$. Here \mathbf{v}^2 indicates an element-by-element function giving the square of each element. Our high-resolution solution is very accurate when Δt and Δx stay small. This is confirmed in Fig. 6(a) where the high-resolution solutions are, at worst, within 10^{-6} of the discretized Cole-Hopf solution for coarse-grainings of $4\times$, and yet better for coarse-grainings of $2\times$ and below. Here, we use $\nu = 0.01$ and $\Delta t = 5 \times 10^{-4}$,

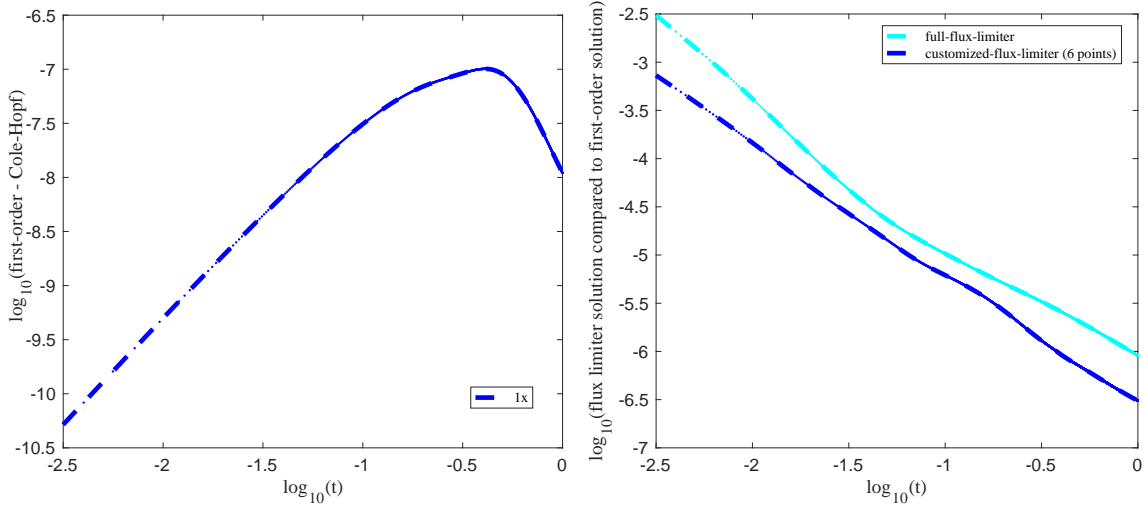


FIG. 6. a): Accuracy of the first-order, high-resolution solution as compared to the Cole-Hopf solution. See Sec. A. b): Relative error between the shock-captured solution computed with $\alpha = \max(|\frac{\partial F}{\partial u}|_u)$ and our customized Lax-Friedrichs flux with fixed $\alpha = 0.6$. See Sec. B

$\Delta x = 5 \times 10^{-3}$ which are the values we used to generate our high-dimensional training dataset.

B. CUSTOMIZED LAX-FRIEDRICHS FLUX

We explored methods to avoid computing the maximum over all u_i when calculating the value of the partial derivative w.r.t. u in Eq. (9). If possible, this would allow us to reduce the training input points in our machine learning method.

We found that replacing $\alpha = \max(|\frac{\partial F}{\partial u}|_u)$ with the constant $\alpha = 0.6$ gave us improved solutions relative to the full flux-limiter when compared to our high-resolution data.

In Fig. 6(b) we plot the relative error between the custom flux limiter and high resolution data compared to the relative error between the full maximum flux limiter and high resolution data for a high resolution simulation with $\Delta x = 2.5 \times 10^{-3}$, $\Delta t = 2.5 \times 10^{-4}$, $\nu = 0.005$. In the plot, we show the average solution error over twenty simulations with random initial conditions. Note that the modified method gives an error that is always less than the standard Lax-Friedrichs method. Therefore, we use this customized flux, f^{low} , with $N_c = 6$ points, which appears in Eq. (17) in our machine learning model.

C. LEARNED FLUX LIMITERS

Our discretized flux ratio bin edges, r_i , and machine learned coefficients, b_i , for flux limiters corresponding to $2\times$, $3\times$, $4\times$, $8\times$ of coarse graining (see Fig. 3(a)) are given in Tables II and III. Note that bin width ($r_i - r_{i-1}$) decreases for small r and increases for large r . Also note that $r_k \sim 1.0$ when $k \sim K/2$, $r_K \sim CG$, and $b_1 \sim CG$.

	r_1	r_2	r_3	r_4	r_5	r_6	r_7	r_8	r_9	r_{10}	r_{11}	r_{12}	r_{13}	r_{14}	r_{15}	r_{16}	r_{17}	r_{18}	r_{19}	r_{20}	r_{21}
2x	0	0.37	0.56	0.68	0.76	0.82	0.87	0.91	0.95	0.98	1.00	1.04	1.07	1.13	1.15	1.21	1.3	1.44	1.73	2.58	10
3x	0	0.29	0.46	0.59	0.68	0.76	0.82	0.88	0.92	0.97	1.00	1.05	1.10	1.15	1.22	1.31	1.44	1.65	2.08	3.34	10
4x	0	0.23	0.40	0.52	0.62	0.71	0.78	0.85	0.91	0.96	1.01	1.07	1.13	1.2	1.28	1.4	1.58	1.85	2.41	4.07	10
8x	0	0.14	0.26	0.38	0.48	0.58	0.67	0.76	0.85	0.94	1.02	1.12	1.22	1.35	1.51	1.73	2.06	2.59	3.64	6.79	10

TABLE II. Discretized space r for $2\times$, $3\times$, $4\times$, and $8\times$ of coarse graining.

	b_1	b_2	b_3	b_4	b_5	b_6	b_7	b_8	b_9	b_{10}	b_{11}	b_{12}	b_{13}	b_{14}	b_{15}	b_{16}	b_{17}	b_{18}	b_{19}	b_{20}
2x	2.33	-1.68	1.17	-0.22	0.36	0.03	0.16	-0.02	0.52	-0.23	0.28	-0.15	0.03	0.09	0.14	-0.04	0.20	-0.08	0.29	-0.09
3x	3.11	-1.63	0.89	-0.08	0.10	0.24	0.08	0.02	0.32	-0.10	0.24	0.02	0.06	-0.07	0.17	-0.04	0.21	-0.06	0.23	-0.14
4x	4.02	-1.81	0.67	-0.04	0.19	0.25	0.12	-0.05	0.37	-0.02	0.12	-0.01	0.11	0.16	-0.01	0.10	0.14	-0.04	0.23	-0.16
8x	7.28	-2.36	0.75	-0.33	0.22	-0.04	0.18	0.16	0.16	-0.04	0.20	0.12	0.06	0.04	0.15	0.10	0.07	-0.02	0.16	-0.30

TABLE III. Line segment slopes b obtained for $K=20$ with $2\times$, $3\times$, $4\times$, and $8\times$ of coarse graining.

Similarly, candidate r_i and b_i for select iterations in the optimization of a discretized machine learned limiter in the region defined by $CG \in [2, 10]$, $K \in [2, 30]$, and $\mu \in [0.01, 0.5]$ (see Fig. 5(a)) are given in Tables V and VI. The corresponding values of CG , K , and μ are given in Table IV.

	CG	K	μ	\bar{C}
0	5x	15	0.075	0.000077
3	3x	29	0.026	0.000058
5	3x	15	0.066	0.000037
7	2x	14	0.037	0.000017
12	2x	11	0.045	0.000011
23	2x	13	0.048	0.000010
26	2x	18	0.047	0.000009

TABLE IV. Coarse graining, CG , number of bins, K , diffusion parameter, μ , and associated cost, \bar{C} , at selected iterations in the optimization of a discretized machine learned limiter in the region defined by $CG \in [2, 10]$, $K \in [2, 30]$, and $\mu \in [0.01, 0.5]$.

D. STANDARD FLUX LIMITERS

See Table VII for the flux limiters used for comparison in Figs. 1 and 2.

[1] Didier Besnard, Francis H Harlow, Rick M Rauenzahn, and Charles Zemach. Turbulence transport equations for variable-density turbulence and their relationship to two-field models. Technical report, Los Alamos National Lab., NM (United States), 1992.

	r_1	r_2	r_3	r_4	r_5	r_6	r_7	r_8	r_9	r_{10}	r_{11}	r_{12}	r_{13}	r_{14}	r_{15}	r_{16}	r_{17}	r_{18}	r_{19}	\dots	r_{29}	r_{30}	
0	0.0	0.29	0.48	0.62	0.73	0.82	0.90	0.98	1.06	1.14	1.24	1.38	1.60	2.04	3.33	10.0							
3	0.0	0.21	0.35	0.46	0.55	0.62	0.68	0.74	0.78	0.83	0.86	0.90	0.93	0.96	0.99	1.02	1.05	1.08	1.11	\dots	4.62	10.0	
5	0.0	0.46	0.66	0.77	0.84	0.90	0.94	0.98	1.02	1.06	1.11	1.17	1.28	1.50	2.12	10.0							
7	0.0	0.54	0.73	0.82	0.89	0.93	0.97	1.00	1.03	1.07	1.12	1.19	1.34	1.78	10.0								
12	0.	0.63	0.80	0.89	0.94	0.99	1.02	1.07	1.13	1.25	1.58	10.											
23	0.0	0.54	0.73	0.83	0.90	0.94	0.98	1.02	1.06	1.12	1.20	1.37	1.84	10.0									
26	0.0	0.49	0.67	0.77	0.84	0.88	0.92	0.95	0.98	1.00	1.03	1.06	1.09	1.13	1.19	1.28	1.47	2.01	10.0				

TABLE V. Discretized bin edge locations, r_i , at select iterations in the optimization of a discretized machine learned limiter in the region defined by $CG \in [2, 10]$, $K \in [2, 30]$, and $\mu \in [0.01, 0.5]$. The corresponding values of CG , K , and μ are found in Table IV.

	b_1	b_2	b_3	b_4	b_5	b_6	b_7	b_8	b_9	b_{10}	b_{11}	b_{12}	b_{13}	b_{14}	b_{15}	b_{16}	b_{17}	b_{18}	\dots	b_{28}	b_{29}	
0	5.33	-2.82	1.67	-0.03	0.26	0.64	0.20	0.06	0.18	0.09	0.05	0.30	-0.01	0.44	-0.08							
3	6.31	-2.87	1.05	-0.22	0.72	0.06	0.29	0.42	0.14	0.15	0.06	0.75	-1.52	2.18	0.24	-0.89	0.77	0.71	\dots	0.37	-0.10	
5	3.42	-2.94	2.69	-0.38	0.50	-0.34	0.35	0.32	-0.71	0.12	0.74	0.44	-0.33	0.68	-0.02							
7	1.88	-1.59	1.42	0.32	0.21	0.06	-0.77	1.15	0.04	-0.08	0.07	-0.07	0.33	0.01								
12	1.75	-1.91	2.37	-0.78	-0.87	0.59	0.36	0.76	-0.33	0.40	0.10											
23	1.91	-1.56	1.61	-0.49	0.10	0.46	-0.53	0.56	-0.55	0.71	-0.24	0.39	0.01									
26	2.26	-1.98	1.95	-0.28	0.48	0.75	-0.41	0.05	-0.01	1.39	0.39	-1.74	1.48	-0.34	-0.01	-0.11	0.56	0.11				

TABLE VI. Line segment slopes, b_i at select iterations in the optimization of a discretized machine learned limiter in the region defined by $CG \in [2, 10]$, $K \in [2, 30]$, and $\mu \in [0.01, 0.5]$. The corresponding values of CG , K , and μ are found in Table IV.

superbee [27]: $\phi_{sb}(r) = \max(0, \min(2r, 1), \min(r, 2))$
monotonized central [28]: $\phi_{mc}(r) = \max(0, \min(2r, 0.5(1+r), 2))$
smart [29]: $\phi_{sm}(r) = \max(0, \min(2r, (1/4 + 3r/4), 4))$
Koren [30]: $\phi_{kn}(r) = \max(0, \min(2r, \min((1/3 + 2r/3), 2)))$
van Leer [19]: $\phi_{vL}(r) = \frac{r+|r|}{1+|r|}$
HCUS [31]: $\phi_{hc}(r) = \frac{1.5(r+|r|)}{r+2}$
ospre [31]: $\phi_{os}(r) = \frac{1.5(r^2+r)}{r^2+r+1}$
UMIST [32]: $\phi_{um}(r) = \max(0, \min(2r, 1/4 + 3r/4, 3/4 + r/4, 2))$
van Albada 1 [33]: $\phi_{va1}(r) = \frac{r^2+r}{r^2+1}$
van Albada 2 [34]: $\phi_{va2}(r) = \frac{2r}{r^2+1}$
symmetric minmod [27]: $\phi_{mm}(r) = \max(0, \min(1, r))$

TABLE VII. Mathematical expressions for the standard flux limiters used for comparison in Figs. 1 and 2

- [2] John D Schwarzkopf, Daniel Livescu, Robert A Gore, Rick M Rauenzahn, and J Raymond Ristorcelli. Application of a second-moment closure model to mixing processes involving multicomponent miscible fluids. *Journal of Turbulence*, (12):N49, 2011.
- [3] Jonathan Tompson, Kristofer Schlachter, Pablo Sprechmann, and Ken Perlin. Accelerating eulerian fluid simulation with convolutional networks. In *Proceedings of the 34th International Conference on Machine Learning-Volume 70*, pages 3424–3433. JMLR. org, 2017.
- [4] Arvind Mohan, Don Daniel, Michael Chertkov, and Daniel Livescu. Compressed convolutional lstm: An efficient deep learning framework to model high fidelity 3d turbulence. *arXiv preprint arXiv:1903.00033*, 2019.
- [5] Balasubramanya Nadiga, Chiyu Jiang, and Daniel Livescu. Leveraging bayesian analysis to improve accuracy of approximate models. *Journal of Computational Physics*, 394:280–297, 2019.
- [6] Henry Chan, Mathew J Cherukara, Badri Narayanan, Troy D Loeffler, Chris Benmore, Stephen K Gray, and Subramanian KRS Sankaranarayanan. Machine learning coarse grained models for water.

- Nature communications*, 10(1):1–14, 2019.
- [7] Johannes Martinus Burgers. A mathematical model illustrating the theory of turbulence. In *Advances in applied mechanics*, volume 1, pages 171–199. Elsevier, 1948.
- [8] Hopf Eberhard. The partial differential equation $ut + uux = \mu u_{xx}$, 1942.
- [9] Julian D Cole. On a quasi-linear parabolic equation occurring in aerodynamics. *Quarterly of applied mathematics*, 9(3):225–236, 1951.
- [10] Henry Wilbraham. On a certain periodic function. *The Cambridge and Dublin Mathematical Journal*, 3:198–201, 1848.
- [11] SK Godunov. A difference scheme for numerical computation of discontinuous solutions of fluid dynamics. *Mat. Sb*, 47:271–306, 1959.
- [12] Bram Van Leer. Towards the ultimate conservative difference scheme. v. a second-order sequel to godunov’s method. *Journal of computational Physics*, 32(1):101–136, 1979.
- [13] Phillip Colella and Paul R Woodward. The piecewise parabolic method (ppm) for gas-dynamical simulations. *Journal of computational physics*, 54(1):174–201, 1984.
- [14] Ami Harten. High resolution schemes for hyperbolic conservation laws. *Journal of computational physics*, 135(2):260–278, 1997.
- [15] Chi-Wang Shu and Stanley Osher. Efficient implementation of essentially non-oscillatory shock capturing schemes, 2. 1988.
- [16] Di Zhang, Chunbo Jiang, Dongfang Liang, and Liang Cheng. A review on tvd schemes and a refined flux-limiter for steady-state calculations. *Journal of Computational Physics*, 302:114–154, 2015.
- [17] Peter K Sweby. High resolution schemes using flux limiters for hyperbolic conservation laws. *SIAM journal on numerical analysis*, 21(5):995–1011, 1984.
- [18] MF Maritz and SW Schoombie. Exact analysis of nonlinear instability in a discrete burgers’ equation. *Journal of Computational Physics*, 97(1):73–90, 1991.
- [19] Bram Van Leer. Towards the ultimate conservative difference scheme. ii. monotonicity and conservation combined in a second-order scheme. *Journal of computational physics*, 14(4):361–370, 1974.
- [20] R. M. Storn and K. V. Price. Differential evolution — a simple and efficient heuristic for global optimization over continuous spaces. *J. Global Optim.*, 11(4):341–359, 1997.
- [21] M. McKerns, P. Hung, and M. Aivazis. mystic: highly-constrained non-convex optimization and uq, 2009-. <https://uqfoundation.github.io/project/mystic>.
- [22] M. McKerns, L. Strand, T. J. Sullivan, A. Fang, and M. Aivazis. Building a framework for predictive science. In *Proceedings of the 10th Python in Science Conference, 2011*, pages 67–78, 2011. <http://arxiv.org/pdf/1202.1056>.
- [23] BB Tripathi, D Espíndola, and GF Pinton. Piecewise parabolic method for simulating one-dimensional shear shock wave propagation in tissue-mimicking phantoms. *Shock Waves*, 27(6):879–888, 2017.
- [24] Ami Harten and Stanley Osher. Uniformly high-order accurate nonoscillatory schemes. i. In *Upwind and High-Resolution Schemes*, pages 187–217. Springer, 1997.
- [25] Xu-Dong Liu, Stanley Osher, and Tony Chan. Weighted essentially non-oscillatory schemes. *Journal of computational physics*, 115(1):200–212, 1994.
- [26] Youngsoo Ha, Chang Ho Kim, Yeon Ju Lee, and Jungho Yoon. Mapped weno schemes based on a new smoothness indicator for hamilton-jacobi equations. *Journal of Mathematical Analysis and Applications*, 394(2):670–682, 2012.
- [27] Philip L Roe. Characteristic-based schemes for the euler equations. *Annual review of fluid mechanics*, 18(1):337–365, 1986.
- [28] Bram Van Leer. Towards the ultimate conservative difference scheme iii. upstream-centered finite-difference schemes for ideal compressible flow. *Journal of Computational Physics*, 23(3):263–275, 1977.
- [29] PH Gaskell and AKC Lau. Curvature-compensated convective transport: Smart, a new boundedness-preserving transport algorithm. *International Journal for numerical methods in fluids*, 8(6):617–641, 1988.
- [30] Barry Koren. *A robust upwind discretization method for advection, diffusion and source terms*. Centrum voor Wiskunde en Informatica Amsterdam, 1993.
- [31] NP Waterson and Herman Deconinck. A unified approach to the design and application of bounded higher-order convection schemes. *Numerical methods in laminar and turbulent flow.*, 9:203–214, 1995.
- [32] Fue-Sang Lien and MA Leschziner. Upstream monotonic interpolation for scalar transport with application to complex turbulent flows. *International Journal for Numerical Methods in Fluids*, 19(6):527–548,

- 1994.
- [33] Gale Dick Van Albada, Bram Van Leer, and WWjun Roberts. A comparative study of computational methods in cosmic gas dynamics. In *Upwind and high-resolution schemes*, pages 95–103. Springer, 1997.
 - [34] MJ Kermani, AG Gerber, and JM Stockie. Thermodynamically based moisture prediction using roe’s scheme. In *4th Conference of Iranian Aerospace Society, Amir Kabir University of Technology, Tehran, Iran*, volume 3. Citeseer, 2003.